VIPAR, a quantitative approach to 3D histopathology applied to lymphatic malformations

René Hägerling,[1] Dominik Drees,[2] Aaron Scherzinger,[2,3] Cathrin Dierkes,[1] Silvia Martin-Almedina,[4] Stefan Butz,[5] Kristiana Gordon,[4] Michael Schäfers,[6,7] Klaus Hinrichs,[3,7] Pia Ostergaard,[4] Dietmar Vestweber,[5] Tobias Goerge,[8] Sahar Mansour,[4] Xiaoyi Jiang,[2,7] Peter S. Mortimer,[4] and Friedemann Kiefer[1,6,7]

[1]Mammalian Cell Signaling Laboratory, Max Planck Institute for Molecular Biomedicine, Münster, Germany. [2]Pattern Recognition and Image Analysis Group, Department of Computer Science, and [3]Visualization and Computer Graphics Group, Department of Computer Science, University of Münster, Münster, Germany. [4]Molecular and Clinical Sciences Institute, St. George's University of London, London, United Kingdom. [5]Department Vascular Cell Biology, Max Planck Institute for Molecular Biomedicine, Münster, Germany. [6]European Institute for Molecular Imaging, University of Münster, Münster, Germany. [7]DFG Cells-in-Motion Cluster of Excellence 1003, Münster, Germany. [8]Department of Dermatology, University Hospital of Münster, Münster, Germany.

BACKGROUND. Lack of investigatory and diagnostic tools has been a major contributing factor to the failure to mechanistically understand lymphedema and other lymphatic disorders in order to develop effective drug and surgical therapies. One difficulty has been understanding the true changes in lymph vessel pathology from standard 2D tissue sections.

METHODS. VIPAR (volume information-based histopathological analysis by 3D reconstruction and data extraction), a light-sheet microscopy–based approach for the analysis of tissue biopsies, is based on digital reconstruction and visualization of microscopic image stacks. VIPAR allows semiautomated segmentation of the vasculature and subsequent nonbiased extraction of characteristic vessel shape and connectivity parameters. We applied VIPAR to analyze biopsies from healthy lymphedematous and lymphangiomatous skin.

RESULTS. Digital 3D reconstruction provided a directly visually interpretable, comprehensive representation of the lymphatic and blood vessels in the analyzed tissue volumes. The most conspicuous features were disrupted lymphatic vessels in lymphedematous skin and a hyperplasia (4.36-fold lymphatic vessel volume increase) in the lymphangiomatous skin. Both abnormalities were detected by the connectivity analysis based on extracted vessel shape and structure data. The quantitative evaluation of extracted data revealed a significant reduction of lymphatic segment length (51.3% and 54.2%) and straightness (89.2% and 83.7%) for lymphedematous and lymphangiomatous skin, respectively. Blood vessel length was significantly increased in the lymphangiomatous sample (239.3%).

CONCLUSION. VIPAR is a volume-based tissue reconstruction data extraction and analysis approach that successfully distinguished healthy from lymphedematous and lymphangiomatous skin. Its application is not limited to the vascular systems or skin.

FUNDING. Max Planck Society, DFG (SFB 656), and Cells-in-Motion Cluster of Excellence EXC 1003.

Conflict of interest: The authors have declared that no conflict of interest exists.

Submitted: May 5, 2017
Accepted: July 14, 2017
Published: August 17, 2017

Reference information:
JCI Insight. 2017;2(16):e93424.
https://doi.org/10.1172/jci.insight.93424.

Introduction

Lymphatic vessels are indispensable for the maintenance of plasma and tissue fluid balance, for tissue immunosurveillance, and for fat homeostasis (1). Tissue fluid homeostasis is dependent on a delicate balance between microvascular filtration (lymph load) and lymphatic resorption (lymph drainage). Disturbances in lymphatic function can contribute to the development of cardiovascular disease, infection,

cancer, and obesity. Impaired lymph drainage specifically results in lymphedema (2). It is only very recently that lymphatic vessels have been considered as an active contributor to these medical conditions (3). A dysfunctional lymphatic system may foster the development of hypertension and atherosclerosis (4, 5), and impaired lymphatic function can predispose affected individuals to bacterial and fungal infections (6).

Despite the severe effect of lymphedema on the quality of life of affected individuals, no curative or molecularly targeted therapy currently exists (7). Lymphedema appears much more common than generally realized (8, 9). It can be caused by accidental or intended trauma to the lymph-draining pathways, e.g., cancer treatment, but there is a hidden lymphedema epidemic, resulting from obesity and poor mobility (10). In addition, worldwide infections, such as filariasis, cause millions of cases, and lymphedema can also be caused by genetic defects. Recent advances in identifying causal genes have also provided information on the function of these genes. Indeed genetic factors may be responsible for the development of many secondary forms of lymphedema, e.g., breast cancer–related lymphedema (11).

A major problem in the clinic is the lack of investigatory tools to understand the mechanisms of lymphedema. The lack of techniques for investigation and diagnosis has been a major contributing factor to a failure to develop effective drug and surgical therapies. Furthermore, limited investigations have also resulted in a failure to discriminate clinically between different phenotypes of lymphedema, making a specific diagnosis more difficult.

The skin histopathology associated with lymphedema has traditionally been analyzed in stained paraffin sections, with a strong emphasis on the prominent aspects hyperkeratosis, fibrotic changes, and inflammatory infiltrations. However, lymphatic vessels are difficult to discern in this setting, and, indeed, the scarcity of imaging modalities for assessment of lymphatic system function and structure has been a significant limitation (7). Larger lymph vessel transport can only be imaged through lymphoscintigraphy and indocyanine green (ICG) lymphography (12, 13). Lymphoscintigraphy provides functional information on lymph transport within a limb but cannot be used to image lymphatic vessels; however, this approach can be used to image the accumulation of tracer within regional lymph nodes within regional lymph nodes. ICG lymphography images the contrast within vessels and not the vessel wall in any detail and can image lymph drainage routes and contractility of the vessels in localized areas (14).

Together, lymphoscintigraphy and ICG lymphangiography provide important information on lymphatic function and gross architecture of collecting lymphatic vessels. Fluorescence microlymphangiography (FML) and intravital dyes can image initial lymphatics within the skin in vivo (15, 16). Intravital dyes are still used to image lymphatic drainage routes to the lymph nodes in order to identify the sentinel node prior to biopsy in cancer management. FML is not a standard investigation in the clinical setting. However, these valuable clinical imaging modalities do not inform on the pathological details of the microcirculation, which are particularly relevant for an assessment of the function of the initial lymphatics.

Such details at subcellular resolution are revealed in histological sections, which allow, through immunohistochemistry using positively identifying antibodies, the unanimous distinction of blood and lymphatic vessels. Due to the limited information contained, extraction of vascular parameters, such as spatial structure, connectivity, and network characteristics, is impossible from the standard 2D sections in cellular pathology. Theoretically the required volume information could be derived by reconstruction of the 3D vascular architecture from serial sections. However, in practice, this approach is extremely labor intensive, and results are often unsatisfactory due to sectioning-associated tissue loss and distortion of the specimen.

Over the last decade, planar illumination or light-sheet microscopy experienced a brilliant renaissance and underwent a rapid technological advancement (17, 18). Light-sheet microscopes generate contiguous series of optical sections from cleared specimen in select cases of up to a cubic centimeter volume. A full representation of the spatial structure of the specimen can be generated by digital reconstruction from these image stacks. Such light-sheet microscopy methods have been successfully used in experimental 3D reconstructions and analysis of developmental processes, the vascular systems, and cancer research (18–22).

We proposed that light-sheet microscopy could be employed to analyze the blood and lymph vessel beds in human tissue samples. We asked the question of whether it was possible to extract characteristic and distinguishing parameters that would, with high confidence, identify pathological alterations. In a feasibility study, we have analyzed skin biopsies from healthy volunteers and a patient suffering from primary lymphedema associated with WILD (warts, depressed cell-mediated immunity, primary lymphedema, and anogenital dysplasia) syndrome (23). To take full advantage of the power of light-sheet microscopy, we combined imaging of immunostained, optically cleared skin biopsies at cellular resolution (mesoscopy)

with computer-based reconstruction and visualization. For further analysis of the lymphatic vasculature, lymphatic vessel structure was recognized by semiautomatic image analysis (segmentation), and characteristic parameters were calculated following nonbiased data extraction. This resulted in a volume information-based histopathological analysis by 3D reconstruction and data extraction procedure, which we refer to using the acronym VIPAR.

Here, we show that, in biopsies from healthy skin, VIPAR distinguished blood and lymphatic vessels with high confidence. The digital 3D reconstruction generated a faithful spatial representation of both vessel beds, which was visually directly accessible and highly informative. Using semiautomated segmentation routines, VIPAR extracted the basic shape and connectivity of the vascular systems, which allowed the subsequent nonbiased determination of fundamental blood and lymph vessel parameters.

Analysis of patient-derived samples from lymphedematous skin and a lymphangiomatous lesion revealed characteristic differences, which were immediately recognizable in the spatial reconstruction. The 3D visualization uncovered abnormalities, such as the fragmentation of lymphatic vessels that were not immediately identifiable in standard 2D histological sections. Importantly, the visually perceptible structural differences in the lymphatic vessels of lymphedematous and lymphangiomatous skin were also reflected in the extracted vessels parameters. Therefore, VIPAR successfully detected and reported disease-associated changes in lymphatic vessel structure.

The light-sheet microscopy–based approach we describe here, VIPAR, is not limited to skin samples but may be applied to all human tissues that can be optically cleared and where suitable whole-mount immunostaining protocols for the target cell population under scrutiny are available. VIPAR provides a straightforward practical route to 3D histopathology, which is capable of bridging the analytical gap between microscopic and macroscopic clinical imaging techniques.

Results

Light-sheet microscopy imaging and computer-based visualization provide a faithful representation of the 3D microvascular anatomy in normal skin. To demonstrate diagnostic potential, we visualized whole-mount immunofluorescence stained human skin biopsies using a LaVision UltraMicroscope II (Supplemental Figure 1, A and B; supplemental material available online with this article; https://doi.org/10.1172/jci.insight.93424DS1). The resulting image stacks comprising approximately 2,000–4,000 optical sections spaced at 1–2 μm distance in z were digitally reconstructed using the volume visualization framework Voreen (Supplemental Figure 1C) (24, 25).

In our volume reconstructions, the endothelial cell–selective adhesion molecule 1 (ESAM1) (26) served as a surrogate marker delineating the position of blood vessels. Albeit expressed on all endothelial cell types, ESAM1 immunoreactivity on lymphatic endothelial cells was comparably weak (Figure 1, A–D). Lymphatic vessels were specifically stained by the mucin-type transmembrane surface protein podoplanin (PDPN) (27) and nuclear expression of the transcription factor prospero homeobox protein 1 (PROX1) (28), both of which allowed identification of lymphatic vessels with high confidence (Figure 1, E–H).

The 3D visualization immediately revealed prominent lymphatic plexuses in the papillary layer (Figure 1C, red arrow) and at the basis of the reticular layer (Figure 1C, green arrow) of the dermis. Both plexuses were connected by discontinuously distributed bundles of blood vessels that often accompanied a lymphatic vessel (Figure 1A and Supplemental Video 1). Looking at the papillary plexus en face through the epidermis, we immediately identified blind-ending lymphatic capillaries (denoted by asterisks in B, F, and H of Figure 1) and areas composed of condensed PROX1-expressing lymphatic endothelial cells (denoted by opposing white arrows in B, F, and H of Figure 1). Such condensations (Figure 1, G and H) were frequently observed next to lymph vessel bifurcations, providing additional evidence for our assumption that they represent lymphatic valves.

In summary, light-sheet microscopic imaging using the UltraMicroscope II (LaVision) and subsequent digital volume reconstruction provided an excellent and immediately interpretable view of the spatial arrangement of blood and lymph vessels in human skin biopsies. However, the exceptionally high level of complexity provided by volume-based analyses of vascular parameters complicates the analysis and its interpretation. Therefore, we wondered if it was possible to automatically extract data on the shape and spatial structure of the vascular systems in an unbiased manner that might aid the assessment and description of the vessel systems as well as the identification of less obvious differences between individual samples, thereby allowing deeper phenotyping of the sample.

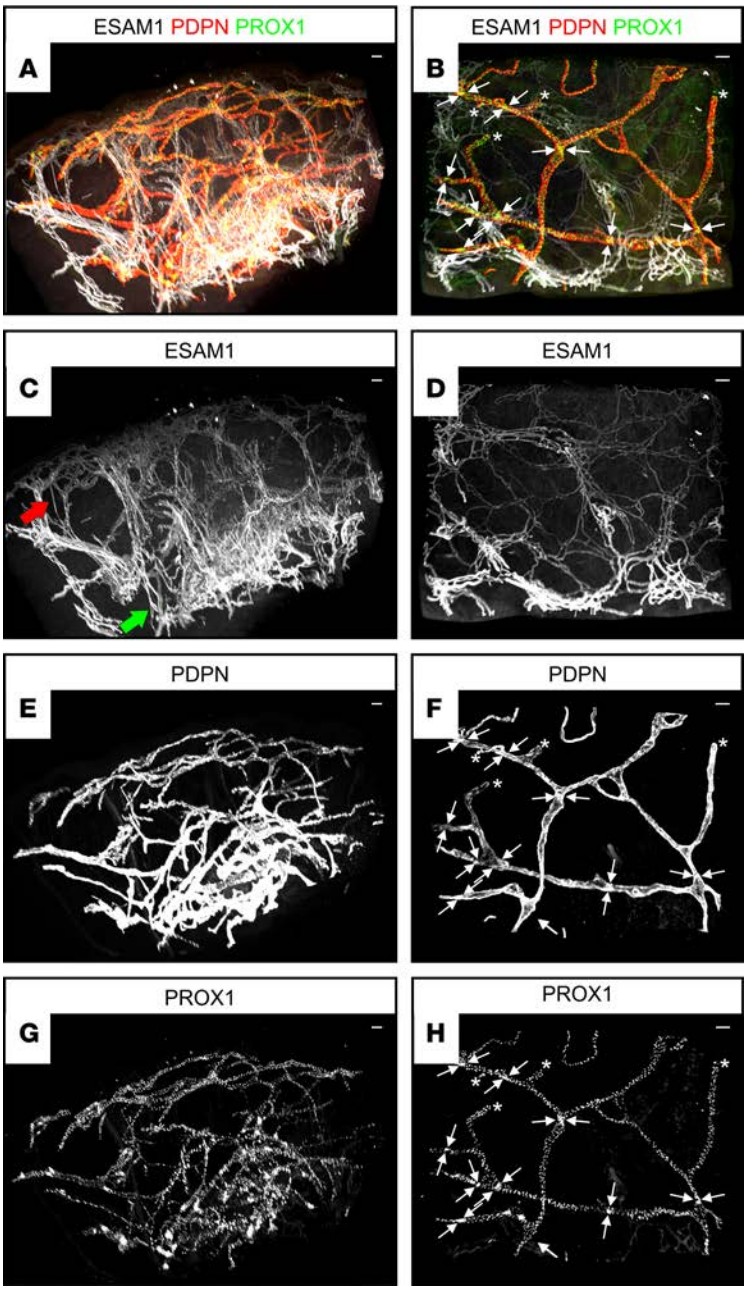

Figure 1. Spatial arrangement of blood and lymphatic vessels in the human dermis visualized by light-sheet–based microscopy. A whole-mount immunostained human skin biopsy from a healthy control was analyzed using light-sheet microscopy (ultramicroscopy). Shown are projections of 3D computer reconstructions generated using the volume visualization framework Voreen. The depicted antigens are indicated in their respective colors on top of the images. ESAM1 served as a general endothelial marker, PROX1 acted as a transcription factor marker, and podoplanin (PDPN) identified lymphatic endothelial cells. (**A**, **C**, **E**, and **G**) Visualization of the tissue volume with the papillary dermis located at top and the cutaneous plexus at the bottom. (**B**, **D**, **F**, and **H**) Digitally rotated view of the same specimen, showing the vessels of the papillary plexus viewed en face through the epidermis. (**A** and **C**) Papillary and cutaneous lymphatic and blood vessel plexuses are distinctly visible (red arrow, papillary plexus; green arrow, cutaneous plexus). (**B**, **F**, and **H**) Valves, identified by condensed high PROX1 expression (between opposing white arrows), were regularly detected in connecting lymphatic (precollector) vessels of the papillary plexus. Blind-ending lymphatic capillaries are marked by white asterisks. Scale bars: 100 μm.

VIPAR, a quantitative approach to histology and histopathology based on 3D reconstruction and volume data extraction. Building on the described light-sheet imaging and visualization procedure, we developed an analytical workflow, which subsequently formed the basis of the 3D tissue reconstruction, comprising three additional basic procedures: (a) segmentation, (b) skeletonization, and (c) feature extraction. We refer to this entire light-sheet–based imaging, visualization, and analysis approach as VIPAR. In an attempt to test the power of VIPAR, we used it for the visualization, 3D reconstruction, and quantitative analysis of the 3D microvascular anatomy in skin biopsies. The deep analysis of the vascular beds by VIPAR, which we report here, is based on semiautomated vessel segmentation followed by extraction of characteristic vascular parameters in a completely unbiased manner (Supplemental Figure 1D).

VIPAR rapidly identifies differences between healthy and pathological skin samples that require elaborate analysis to be revealed by standard histopathology methods. To test the capacity of VIPAR to distinguish healthy from disease-affected tissue and possibly identify pathologies, we analyzed not only multiple samples of healthy skin, but also lymphedema and lymphangiomas skin samples. Diseased samples were derived from a 33-year-old Asian male patient with WILD syndrome (Supplemental Figure 2, A–D) and lymphedema of the left arm and leg (Supplemental Figure 2, A and B). Lymphatic drainage on the left side of the body was severely diminished, basically resulting in a complete functional lymph vessel aplasia (Supplemental Figure 2C). In addition to lymphedema, there was a large papillomatous and pedunculated lesion on the left heel, which clinically represented a lymphangiomatous change (Supplemental Figure 2, E–G). We therefore compared 3 skin biopsies: (a) normal skin (calf) from three healthy volunteers, (b) lymphedema skin (calf), and (c) the lymphangiomatous skin nodule.

We compared the analytic power of VIPAR with an assessment of the affected lesions using traditional 2D histological sections. We therefore immunostained 10-μm cryosections with antibodies directed against ESAM1, PDPN, and the lymphatic vessel endothelial hyaluronan receptor 1 (LYVE1) (29). Sections were either derived from skin of a healthy leg (Figure 2A) or from lymphedematous skin from the leg (Figure 2, B and C). As noted before, ESAM1 was preferentially expressed on blood vessels, while LYVE1 and PDPN together reliably marked the lymphatic vasculature. Control skin showed the presence of blood

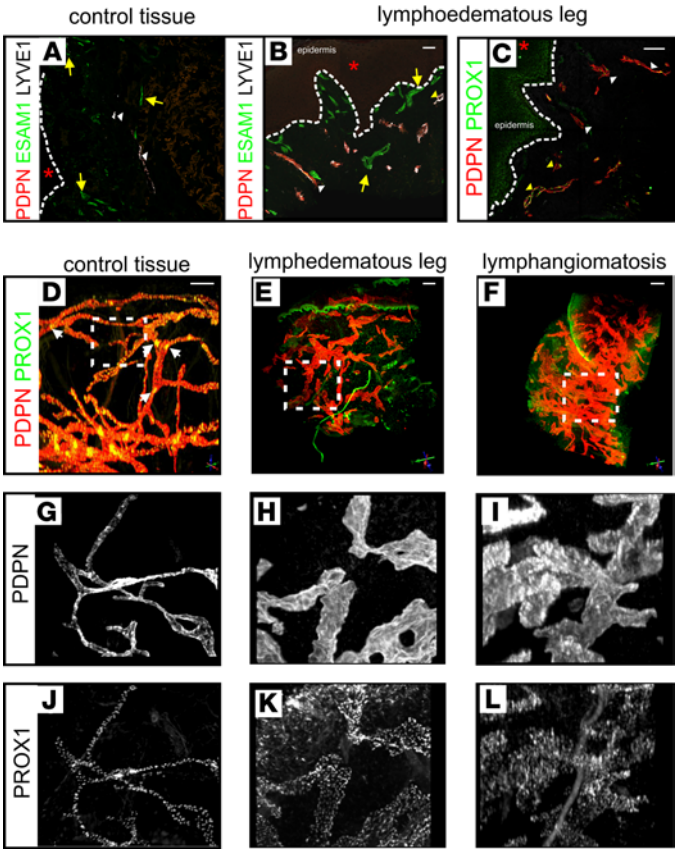

Figure 2. Light-sheet microscopy–based analysis of healthy and diseased skin biopsies reveals lymph vessel defects that are unrecognizable in microtome sections. (**A**–**C**) Immunohistological detection of vascular markers in microtome sections of healthy control (**A**) and patient (**B** and **C**) lower limb skin biopsies. ESAM1, endothelial marker; PDPN, LYVE1, and PROX1, lymphatic-specific endothelial markers. Lumenized blood (yellow arrows) and lymphatic vessels (white arrowheads) are indicated. Dashed line depicts the border between epidermis (indicated by red asterisks) and dermis. Scale bars: 100 μm. (**D**–**L**) Maximum intensity projections of image stacks derived by light-sheet microscopy (UltraMicroscope II) of whole-mount immunostained control (**D**, **G**, and **J**) and patient skin biopsies (**E**, **F**, **H**, **I**, **K**, and **L**). Image stacks were rendered using the volume visualization framework Voreen. Detected antigens and respective colors are indicated. (**D** and **F**) Lymphatic valve areas (identified by high PROX1 expression) are marked by white arrows; valve areas were absent in patient biopsies (**E** and **F**). Specimens are depicted such that the epidermal layer is located on the top of the picture (red asterisks). Note acanthosis and hyperkeratosis in patient biopsy (**B** and **C**). Scale bars: 100 μm.

capillaries (2.1% of total section area) as well as lumenized lymphatic vessels (0.4% of total section area) (Figure 2A). In comparison, in the biopsy derived from the lymphedema-affected leg, both blood and lymphatic vessel beds appeared dilated, which was associated with an increase in the area occupied by blood (3.1% of total section area) and lymphatic (2.4% of total section area) vessels (Figure 2B). In the sections, lymphatic vessels appeared without exception lumenized, which is indicative of fluid uptake and does not provide hints toward the underlying pathology. We further confirmed this finding in anti-PDPN– and anti-PROX1–stained sections, which also unambiguously displayed lumenized lymphatic vessels (Figure 2C).

As a first step in comparing 2D histology and VIPAR, we probed the light-sheet microscopy–based approach by comparing three identically stained skin biopsies from the legs of three healthy individuals (one representative example of the three is shown in Figure 1 and Figure 2, D, G, and J) with the lymphedema-affected leg sample (Figure 2, E, H, and K) and with the lymphangiomatous sample (Figure 2, F, I, and L). In agreement with the histopathological analysis (Figure 2, A–C), the volume reconstruction, which is part of VIPAR, immediately revealed a hyperplasia of the lymphatic vessels (compare Figure 2, D and G, to Figure 2, E and H, and Figure 2, F and I). The lymphatic vessel volume per tissue volume was increased from about 1.1% in the control samples to 2.7% in the lymphedema sample and 4.9% in the lymphangiomatous sample. However, in contrast to standard 2D section–based histology, which had simply identified an increase in lumenized lymphatic vessels, VIPAR, in addition, revealed a high number of hyperplastic but also disrupted, isolated lymphatic vessel fragments in the lymphedematous sample (Figure 2E and Supplemental Video 2). Such vessel fragments can be expected to be nonfunctional for lymphatic drainage and may therefore have contributed to the developing clinical symptoms. Lymph vessels fragmentation was specific for the lymphedematous biopsy and not seen in the lymphangiomatous sample with strong hyperplasia (Figure 2F and Supplemental Video 3). In both biopsies affected by lymph vessel abnormalities, the clear distinction between the papillary and reticular basal lymphatic plexus was no longer possible. In addition, we were struck by the apparent absence of condensed areas of PROX1-expressing lymphatic endothelial cells, suggesting a lack or deterioration of lymphatic valves in the precollecting lymphatic vessels (Figure 2, D–F).

Characteristic differences of lymphatic vessels in healthy and pathologic skin samples were reliably detected by VIPAR. 3D reconstruction of the PDPN-positive lymphatic vasculature revealed immediately recognizable differences between healthy skin and both the lymphedematous and lymphangiomatous skin biopsies (Figure 3, A–C). We now wondered if these differences were maintained during vessel segmentation and could be quantified following the automated data extraction implemented in VIPAR.

For segmentation of the lymphatic vessels, we applied an interactive semiautomatic random walker approach (30) to a downsampled version of the PDPN-positive channel comprising stacks of up to 4,000

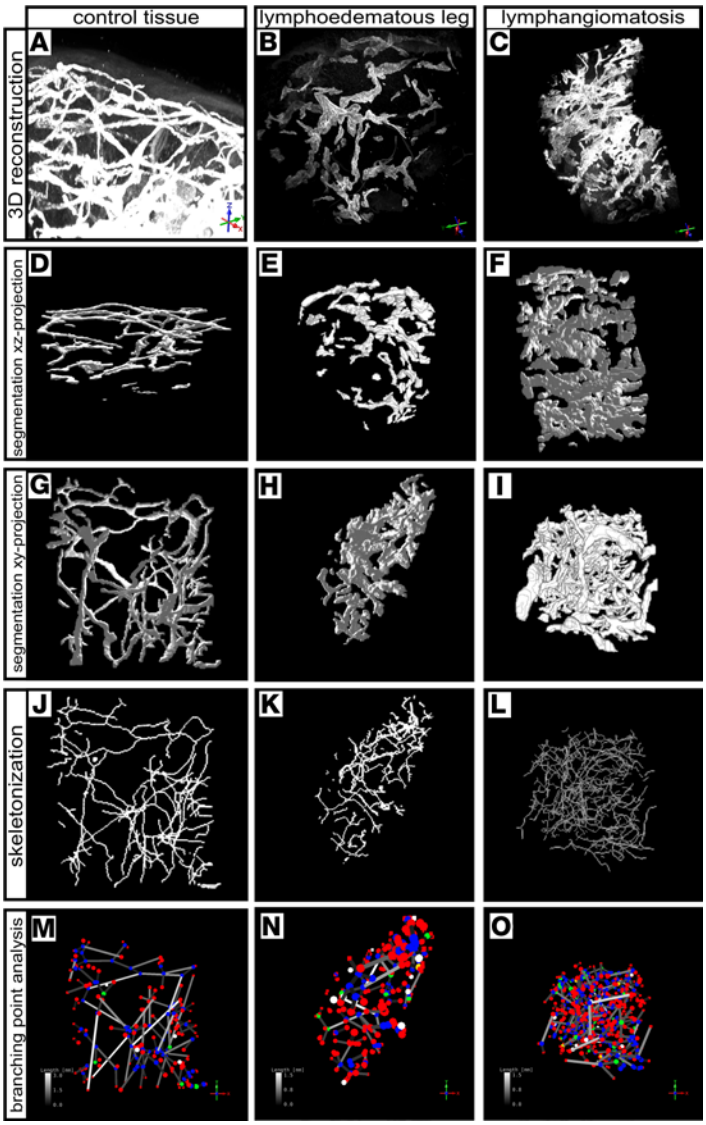

Figure 3. Automated segmentation of the lymphatic vasculature in digital 3D volume reconstructions of control and patient skin biopsies. Skin biopsies whole-mount immunostained for PDPN were subjected to light-sheet–based microscopy (UltraMicroscope II), and the obtained image stacks were visualized using the volume visualization framework Voreen (**A**–**C**, also shown in Figure 2, D–F). Lymphatic vessel surfaces were extracted from the volume reconstruction by automatic segmentation of a subvolume using a random walker approach, followed by postprocessing. Spatial 3D renderings of the specimen are shown from a lateral view where the epidermis is located atop the depiction (*xz* projection, **D**–**F**) and following a virtual 90° rotation around the *x* axis, from the en face view of the skin, i.e., seen through the epidermis (*xy* projection, **G**–**I**). In the control sample, this view largely corresponds to the lymphatic vessels of the papillary plexus. Subsequently vessels were skeletonized (**J**–**L**), followed by detection and classification of the branching points of the vessel convolutes (colored dots in **M**–**O**). The rotational position of the rendered specimen in space is indicated by the axis indicators in the panels.

optical sections (Figure 3, A–C). Subsequent skeletonization, branching point analysis of the lymphatic morphology, and data extraction of markers potentially distinguishing healthy and pathological samples were performed in a nonbiased, fully automatic fashion. 3D visualization following the segmentation of lymph vessels indicated that differences in density, volume, and organization of the lymphatic vasculature were maintained during the segmentation process. The irregularly formed vessel fragments characteristic of the lymphedematous biopsy and the strong hyperplasia of the lymphangiomatous sample were easily visually recognizable in the segmented vessel representation (Figure 3, D–I).

For a quantitative assessment of changes in the pathological sample, we used the extracted skeleton (Figure 3, J–L), which was based on the binary image generated by segmentation, to calculate characteristic topological features, including the branching points of lymphatic vessels and their connectivity (Figure 3, M–O). Besides the branching point distance, the length of the connecting segments, and the segment volume (Supplemental Figure 3, A and B), we computed additional morphological features, including average radius, roundness (i.e., the ratio between the surface voxels with the largest and smallest distance to the medial axis in the cross section), and straightness of the lymphatic vessel segments (for definitions of the calculated parameters, see Supplemental Figure 3, A–C). A correlation plot depicting Pearson's correlation coefficient for the automatically extracted vascular parameters is shown in Supplemental Figure 4. Segment length, distance, and volume showed the highest correlation, suggesting that these parameters describe different aspects of the same or related structural alterations. In the vessel connectivity analysis, we classified each vascular branching point according to the number of vessel segments connected to this particular node (Supplemental Figure 3D). Oblong vessel fragments were classified as a segment delimited by two nodes of branching degree one, as the edges of these segments were formed by two nodes extending one branch each. For sphere-like-shaped small vessel fragments, the two nodes are close together, such that they, due to the limited image resolution, degrade to a single node and were consequently classified as a node of branching degree zero, since no branches extend from these fragments. Branching points with a connectivity of two, which may be generated as an artefact by the current version of the graph extraction algorithm were not considered in this analysis, as they do not represent a true vessel node or branching point in the system (Supplemental Figure 3D). For all other vessel segments, the number of branches extending from each edge node was determined as the branching degree (Supplemental Figure 3D). The global branching point analysis then classified all nodes in the volume according to their branches (Figure 4G). In addition,

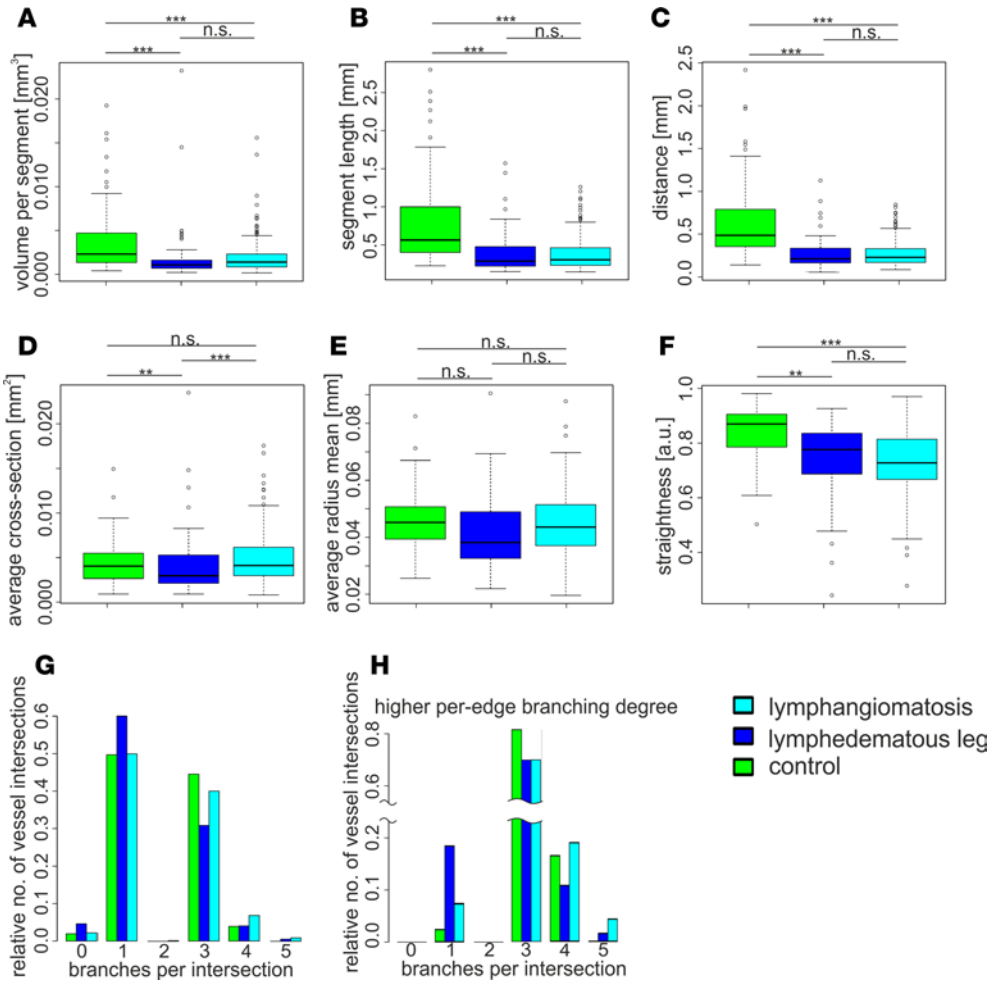

Figure 4. Quantitative parameters distinguish the lymphatic vascular network in control and patient skin biopsies following automated extraction of vessel shape and connectivity characteristics. Parameters that distinguished the control sample (n = 1) from the lymphedematous (n = 1) and lymphangiomatosis sample (n = 1) were calculated from automatically extracted vessel shape and connectivity data. (**A**–**F**) The line in the box-and-whisker plots in represents the median, the boxes represent the upper and lower quartile, and the end of the whiskers represent the 1.5-fold interquartile range. (**G** and **H**) Results of the connectivity analysis for (**G**) total branching point degree and (**H**) the higher per-edge branching degree. The total branching point analysis is cantered on the spheres forming each node, while the higher degree per-edge analysis for each segment considers the maximum branching degree of both connected nodes. A total branching point degree of zero therefore represents spherical vascular elements, whereas a higher per-edge branching degree of one represents the number of elongated, nonconnected, nonbranched vascular elements. Note the decreased segment length and distance in lymphedema- and lymphangiomatosis-affected samples as well as the increased number of spherical and elongated, nonbranched vessel elements in the lymphedematous sample. Supplemental Figure 3 provides an overview of the definitions of the extracted parameters depicted in Figure 4. Mann-Whitney U test with a Bonferroni correction for multiple comparison was used to compare data between groups. $^{**}P < 0.01$, $^{***}P < 0.001$.

for each segment, the higher and lower (per-edge) branching degrees were defined as the maximum/minimum branching degree of the two nodes connected by the segment. The distribution of higher branching degree for all branches is shown in Figure 4H.

A selection of parameters that were significantly different between healthy and the two different diseased samples from the patient investigated here are depicted in Figure 4. Segment volume (46.6%, $P < 0.001$ and 55.7%, $P < 0.001$) (Figure 4A), segment length (51.3%, $P < 0.001$ and 54.2%, $P < 0.001$) (Figure 4B), and branching point distance (43.5%, $P < 0.001$ and 49.1%, $P < 0.001$) (Figure 4C) were significantly reduced in the lymphedema and lymphangiomatous sample, respectively. Vessel average cross section (75.1%, $P < 0.001$) (Figure 4D) was also reduced in the lymphedematous, but not in the lymphangiomatous, sample (102.0%, NS). Average vessel radius was not significantly altered compared with control skin (Figure 4E). Straightness (89.2%, $P = 0.009$ and 83.7%, $P < 0.001$) (Figure 4F) and roundness (data not shown) were again significantly reduced in both,the lymphedematous and lymphangiomatosis sample. In addition, the connectivity analysis revealed distinctive differences between healthy and diseased samples.

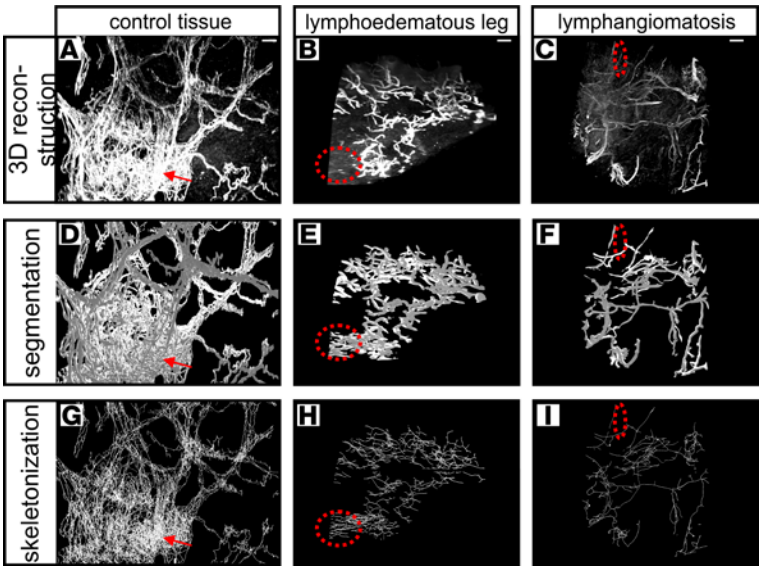

Figure 5. Automated segmentation of the blood vasculature in digital 3D volume reconstructions of control and diseased skin biopsies. (**A**–**C**) Digitally generated spatial reconstructions of image stacks obtained by light-sheet–based microscopy (UltraMicroscope II) of skin biopsies, which were whole-mount immunostained for ESAM1. Biopsies were either from the lower leg of a healthy control (**A**, **D**, and **G**) or lymphedematous leg skin (**B**, **E**, and **H**) or a lymphangiomatous skin biopsy (**C**, **F**, and **I**). Scale bars: 100 μm**.** Computer reconstruction and rendering was performed using the volume visualization framework Voreen. (**D**–**F**) Identified by ESAM1 immunostaining, the blood vascular network was segmented in a semiautomated fashion and is represented by digital volume rendering. (**G**–**I**) Following skeletonization, an automated determination of vessel branching points the vascular network was performed allowing a classifying node analysis. Note the exceptional level of complexity within the healthy control tissue sample that was still successfully segmented, skeletonized, and analyzed for automated data extraction. Areas of high background signal intensity (**B**, **E**, and **H**, red broken circle) can result in false-positive signals, while a low foreground signal (**C**, **F**, and **I**, red broken ellipse) may result in false-negative segmentation results.

Compared with the control biopsy, in both samples derived from the patient, the number of elongated but disconnected lymphatic vessel fragments was increased. The lymphedematous sample was, however, more strongly affected (Figure 4H). Interestingly, small, isolated spherical vessel fragments were limited to the lymphedematous sample (2.38-fold increase) (Figure 4G).

Taken together, in our data sets, distinguishing differences in vessel structure and connectivity were maintained during VIPAR-based skeletonization and data extraction. Hence, VIPAR was able to reliably reveal distinguishing differences between healthy and two different diseased biopsies. Identification of parameters that report robust differences between healthy and lymphedematous samples and, hence, would demonstrate the diagnostic power of VIPAR will require the analysis of a larger patient collective.

VIPAR is a generally applicable tool for the analysis of histological samples. Having demonstrated the power of VIPAR for the histopathological analysis of the dermal lymphatic vasculature, we wanted to extend this approach to dermal blood vessels to demonstrate its general applicability. As shown in Figure 1, multicolor immunostaining for lymphatic-specific markers (PROX1 and PDPN) and the surrogate blood vascular marker (ESAM1) provided a clear distinction of both vascular systems, enabling the simultaneous analysis of blood and lymphatic vessels in the same specimen.

Assessment of the blood vasculature was based on ESAM1 immunostaining (Figure 5, A–C). Blood vessels were segmented semiautomatically by computing Hessian vesselness features on multiple Gaussian scales (31), followed by manual global thresholding to obtain a binary image and postprocessing to remove small segmentation artefacts. The segmented vessel structures were represented as binary volume (Figure 5, D–F), and, for subsequent skeletonization, the medial axis within each vessel was computed using the voxel-thinning method (Figure 5, G–I) (32). The topology of the resulting vessel network was extracted by identification of branching points and skeleton voxels that belong to vessel segments based on the definitions of Klette (33). Connectivity analysis and the extraction of morphological features were performed as described for lymphatic vessels.

Despite the high level of precision achieved during segmentation, we also noted limitations of the applied algorithms, particularly associated with a low signal-to-noise ratio of the imaging data, resulting in segmentation artefacts (Figure 5, B, C, E, F, H, and I, red dashed circles and ellipses). Segmentation errors due to high background or low signals led to the addition of false-positive vessel structures (Figure 5, B, E, and H) as well as the loss of nonsegmented vessels (Figure 5, C, F, and I), respectively.

3D microanatomy of the dermal blood vasculature and alterations in lymphatic pathologies. 3D reconstruction of the healthy dermal blood vessels (Figure 3A) revealed a highly branched, complex-shaped vascular network. Capillaries of the papillary plexus (Figure 1C, red arrow) were served and drained by larger vessels that traversed the dermis connecting to the reticular basal network (Figure 1C, green arrow). In addition, dermal glands were surrounded by a particularly intense blood vascular plexus (Figure 5, A, D, and G, red arrow).

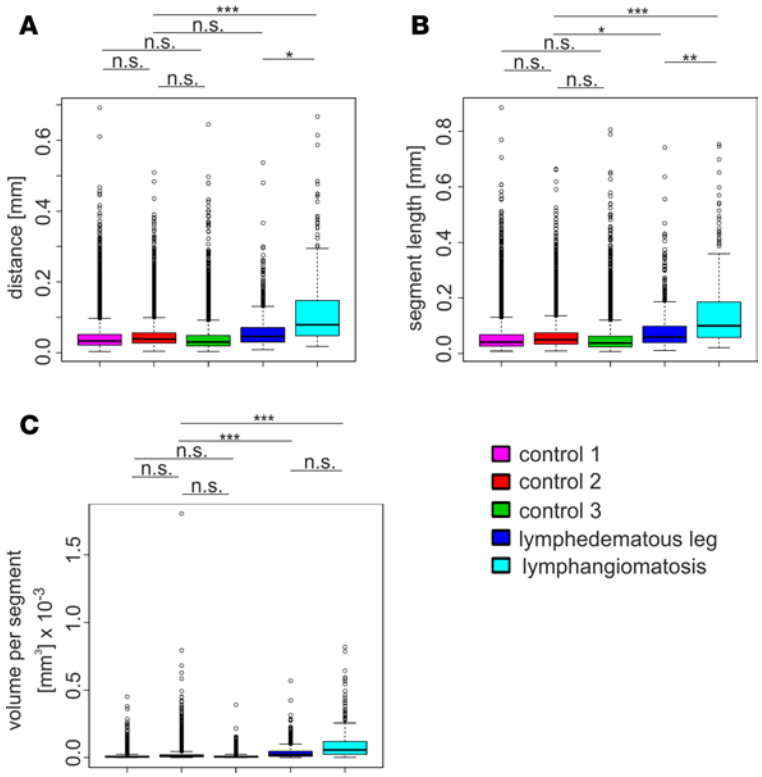

Figure 6. Determination of distinguishing characteristic parameters of the blood vessels in healthy and patient samples. Following segmentation and skeletonization, the segment properties of the blood vasculature in three different control skin biopsies (n = 3), the lymphedematous skin biopsy (n = 1), and the lymphangiomatous skin biopsy (n = 1) were quantified, according to the definitions provided in Supplemental Figure 3. (**A**) Distance describes the length of the direct connection between branching points. (**B**) Segment length corresponds to the length of the center line of a vessel between two branching points. (**C**) The volume of the corresponding vessel segment is calculated from the total number of voxels associated with the segment. The vessel cross section is calculated as the quotient of volume and length. Data are presented as box-and-whisker plots, with the line depicting the median, the boxes showing upper and lower quartile, and the end of the whiskers representing the 1.5-fold interquartile range. Note the increased segment length and distance in lymphedematous and lymphangiomatous skin biopsies. Mann-Whitney U test with a Bonferroni correction for multiple comparison was used to compare data between groups. *P < 0.05, **P < 0.01, ***P < 0.001.

Overall, we analyzed the blood vessels in skin samples from three healthy individuals. Comparable staining intensity, patterning, and morphological vascular parameters, including segment length, distance, and volume indicated a high degree of reproducibility of VIPAR (Figure 6, control 1–3).

In contrast to the mild increase in blood vessel density of 2.1%–3.1% of the total area measured by histopathological analysis in the lymphedematous sample (Figure 2, A and B), 3D reconstruction and analysis by VIPAR revealed a decrease in blood vessel density as well as a reduced network complexity associated with both lymphedema and lymphangiomatosis (Figure 5, B and E, as well as Figure 5, C and F). In addition, in the blood vasculature, the structured hierarchic organization of the papillary and reticular plexuses and their connections were absent. Blood vessels in the lymphangiomatous papule appeared to be dilated. In contrast to the lymphatic system, branching point distance, segment length, and segment volume in lymphedematous and lymphangiomatosis-affected tissue were all significantly increased as compared with the controls (Figure 6). This was more pronounced in lymphangiomatosis-affected (2.4-fold distance, 2.4-fold segment length, 7.4-fold volume) as compared with lymphedematous (1.4-fold distance, 1.4-fold segment length, 2.9-fold volume) tissue. The difference between distance and segment length was highly significant between lymphedematous and lymphangiomatosis-affected tissue (Figure 6, A and B), while the difference in segment volume was less significant (Figure 6C). In addition, the increase in branching point distance between controls and the lymphedematous sample was only slight (Figure 6A).

Taken together, VIPAR proved to be suitable for the analysis of both vascular systems in human skin samples. It reliably detected visually obvious defects and allowed a quantitative assessment of the pathological states lymphedema and lymphangiomatosis following nonbiased data extraction and calculation of morphological parameters.

Discussion

In this study, we demonstrate the feasibility of combining light-sheet microscopy and computer-aided visualization with semiautomated segmentation and nonbiased data extraction to analyze human tissue biopsies.

We performed VIPAR on biopsies of healthy human skin. VIPAR produced a faithful, digital high-resolution 3D representation of the blood and lymphatic vessel beds, which was directly accessible to visual interpretation. The 3D visualization in VIPAR is based on the Voreen visualization framework (24, 25), which allows full digital repositioning of the specimen and, hence, inspection from any viewing

angle and at any magnification up to the microscopic resolution limit. Dermal capillary plexuses in the biopsy samples plus specific details, such as details of the initial lymphatics and lymphatic valves, were readily recognizable.

Full volume information for both the blood and lymphatic vessel beds allowed semiautomated segmentation and, hence, the extraction of fundamental shape and connectivity parameters. In a subsequent data analysis, characteristic properties, such as the distance between vessel branching points and average volume or length of vessel segments, were calculated. This part of the analysis was performed in an automated and therefore nonbiased manner. It was based on all vessel segments present in the entire sample volume analyzed.

We applied this procedure to three biopsies of healthy control skin and observed a high consistency of the derived vascular parameters, demonstrating the robustness of the technique. This encouraged us to probe the capacity of VIPAR to identify alterations in two diseased skin biopsies obtained from a WILD syndrome patient representing lymphedematous and lymphangiomatous skin. Differences in vessel structure compared with healthy biopsies were immediately obvious in the lymphedematous sample. The presence of isolated, albeit lumenized lymphatic vessel fragments was a distinguishing feature that had previously not been identified in this patient before. In histological sections, the missing spatial information in the *z* dimension precluded recognition of such fragments, which cannot be distinguished from contiguous, patent vessels running perpendicular to the sectional plane. The lymphangiomatous skin biopsy revealed only little fragmentation but a strong hyperplasia of the lymphatic vasculature.

The pathological alterations and underlying structural changes that were readily visible in the 3D visualization were also reflected in the subsequent data analysis, as the diseased samples displayed significantly changed vascular properties.

The presence of isolated lymph vessel fragments in the lymphedema skin was reflected in the branching analysis, which revealed an increased frequency of segments with zero branches, i.e., spherical fragments, and one branch, i.e., oblong fragments, in the total analysis and, even more strikingly, of segments with one branch per intersection in the higher per-edge branching degree analysis.

We have presently no data on the appearance of disrupted lymphatic vessels in the patient's etiology of lymphedema. It would, however, seem plausible that the disruption of lymphatic vessels may have been caused by increasing mechanical strain within edematous tissue. Once present, disrupted lymph vessels may have facilitated edema development or aggravated preexisting latent edema. This could have been a contributing factor to the delayed manifestation of the disease in the patient. A robust and quantitative analytic approach such as VIPAR could aid in defining a threshold for the start of potential future treatment, long before the advent of clinically manifest symptoms.

The most distinguishing feature of a sample derived from a lymphangiomatous papule of the WILD patient was the lymph vessel hyperplasia, which was reflected in a 4.36-fold increase of lymph vessel volume per tissue volume compared with healthy skin. Remarkably, the segment length (0.47-fold [lymphedema], 0.50-fold [lymphangiomatosis] of control biopsy) and, hence, branching point distance (0.48-fold [lymphedema], 0.51-fold [lymphangiomatosis] of control biopsy) of lymphatic vessels were significantly decreased in both samples with lymphatic abnormalities. Despite the strong lymphatic hyperplasia, i.e., vessel distension in the lymphangiomatous sample, the overall result of the simultaneous shortening of vessel fragments was a reduction of the volume per lymph vessel segment. We interpret the finding that concomitantly the vessel straightness was reduced as an indication that the lymphatic vessels have reacted to mechanical stretch by extension, very likely through proliferation and increased branching. In contrast, segment distance and length were increased for blood vessels, which would argue that the vessel bed was distended by the edema and responded less efficiently by vascular remodelling.

The large spectrum of parameters that can be derived by VIPAR has to be carefully screened for parameters that will be significantly altered in the context of a given pathology. Identification of such parameters would establish VIPAR as a diagnostic tool (Supplemental Figure 4). In our analysis of the lymphatic vessel system, the volume information-based analysis of skin biopsies compared very favorably with the analysis of histological sections.

Transition from the analysis of single histological planes to the tissue volume-based VIPAR approach is associated with a massive increase in the amount of evaluated data, which resulted in elimination of the variability inevitably introduced by the arbitrary nature of sectional planes in standard 2D histology and enabled the recognition of phenomena that can be identified far easier and faster in 3D

structures. Such pathological, structural alterations were faithfully and quantitatively reflected in the extracted descriptive tissue parameters.

Not too surprisingly, the quality of the achieved vessel segmentation was directly correlated with the quality of the acquired image data. In that respect, we encountered rare false-positive results caused by the misinterpretation of autofluorescent background extracellular matrix components and also the failure to detect very dimly stained vessels of small physical dimensions. Future approaches to minimize these issues may entail the development of improved antibodies and staining protocols, more sensitive microscopic image acquisition, and, most importantly, refinement of the segmentation algorithms. The analysis we describe here relies on the availability of whole-mount immunostaining protocols for the structure or cell type under investigation and on subsequent tissue clearing. Recently, a clearing protocol that is compatible with a wide variety of antibodies for immunostaining has been described (34). Alternatively, a variety of protocols that retain the fluorescence of genetically encoded fluorescent proteins have become available (35, 36). An obvious cost for the analytical power provided by the VIPAR is the massive amount of imaging data that need to be handled and evaluated, which presently still require a high-performance graphic work station for efficient application. Although decreasing costs for computer memory and data storage should rapidly make this approach more affordable, transfer, analysis, and archiving of large-volume light-sheet data remains a challenge. For the light-sheet microscopic observation of developmental processes in drosophila and zebrafish, efficient projection algorithms have been designed, resulting in substantial data reduction (37). However, in these cases, only the surface of the developing organisms is of interest, while, for VIPAR, the entire tissue volume must be analyzed, which limits the possible data reduction.

In conclusion, (a) the unique strength of the VIPAR approach is that it allows a markedly deeper phenotyping of tissue samples than the presently available standard 2D analysis of sections. We have shown here that compared with healthy skin biopsies, skin samples associated with lymphatic vessel disorders showed significant differences in their segment length, segment distance, volume per segment, volume of lymphatic vessels per tissue volume, and their vessel connectivity, as shown by branching point analysis. (b) The VIPAR approach reduces experimental bias through the automated parameter extraction of VIPAR. However, for different pathologies the best outcome parameters will have to be defined. (c) Additionally, the VIPAR approach may provide novel insights into the mechanisms of disease development and, hence, help patient stratification or guide specific treatment once the optimal outcome parameters have been defined. In the context of dermal vascular lymphatic diseases, deep phenotyping using VIPAR will provide additional criteria for the diagnostic algorithm for primary lymphatic dysplasia and possibly aid the identification of genetic defects in patients (38).

The VIPAR approach is not limited to the analysis of vascular structures but can be more widely applied to suitable tissue biopsies of up to 1-cm^3 volume. It substantially enhances the detection of structural defects and alterations in tissues with a spatially complex arrangement. As it is based on mesoscopic light-sheet microscopy, VIPAR also bridges the scales between high-resolution microscopy and whole-body imaging. We believe that VIPAR has the potential to open a new field of 3D pathology.

Methods

Light-sheet microscopy. After immunofluorescence whole-mount staining, optically cleared skin biopsies were imaged using a LaVision UltraMicroscope II (LaVision BioTec). Stacks were captured with a step size of 1 or 2 μm and at different magnifications. 3D reconstruction, analysis, and segmentation and calculation of vascular parameters of ultramicroscopy stacks were performed using custom software leveraging the Voreen framework (24, 25).

Antibodies. The following antibodies were used: rabbit polyclonal anti-human PROX1 (102-PA32, RelaTech), goat polyclonal anti-human PROX1 (AF2727, R&D Systems), goat anti-human LYVE1 (AF2089, R&D Systems), mouse anti-human PDPN (clone D2-40, Dako), and mouse anti-human PECAM1 (clone 89C2, Cell Signaling Technologies). Rabbit antibodies recognizing the extracellular domain of human ESAM1 were raised against an ESAM1-Fc (ESAM-IgG1) fusion protein, produced in stably transfected CHO cells. Antigen-specific antibodies of the serum (VE50) were affinity purified with ESAM1-Fc immobilized on CnBr-Sepharose (GE Healthcare); antibodies against the IgG1 Fc part were removed by incubation with immobilized human IgG.

Immunofluorescence skin biopsy whole-mount stainings. Fresh skin biopsies were fixed for 4 hours in 4% PFA/PBS at 4°C. After permeabilization (0.5% Triton X-100/PBS), the samples were blocked in PermBlock

solution (1% BSA, 0.5% Tween 20 in PBS), and whole-mount stainings were performed using anti-PECAM1, anti-ESAM1, anti-PROX1, anti-PDPN, and anti-LYVE1 primary antibodies and Alexa dye–coupled secondary antibodies (Life Technologies) diluted in PermBlock. Following each staining step, samples were washed three times in PBS-T (0.1% Tween 20/PBS).

Optical clearing of skin biopsies. Optical clearing of tissue samples was described before (39). Briefly, whole-mount stained skin biopsies were embedded in 1% low-melting-point agarose. After dehydration in methanol (50%, 70%, 95%, >99.0%, >99.0% [v/v] methanol, each step 30 minutes), samples were optically cleared in a benzyl alcohol/benzyl benzoate solution (BABB, ratio 1:2 [v/v]) for 4 hours twice. Cleared samples were stored in BABB and imaged using a LaVision UltraMicroscope II (39, 40).

Immunohistochemistry. Skin biopsies were fixed for 4 hours in 4% PFA/PBS, washed in PBS, embedded and snap-frozen in OCT. 10 μm and 20 μm cryosections were fixed in 4% PFA for 15 minutes, washed and blocked (10% chicken serum, 0.3% Triton X-100 in PBS). Subsequently, sections were incubated for 1 hour with primary antibodies (diluted in 1% BSA, 1% chicken serum, 0.3% Triton X-100 in PBS), washed three times in PBS-T and finally incubated in Alexa dye–conjugated secondary antibodies (Life Technologies). After sample mounting in Mowiol (Calbiochem, 475904), confocal images were captured using a Zeiss LSM 780 (×20, NA = 0.8 and ×63 oil, NA = 1.4) confocal microscope.

Image processing and analysis. For analysis of lymphatic and blood vessel properties, we integrated our processing pipeline into the volume visualization framework Voreen (Volume Rendering Engine) (24), which has been extended to allow the visualization of large image stacks (25). The analysis workflow consists of the three basic steps: segmentation, skeletonization, and feature extraction. For segmentation of the lymphatic vessels, an interactive semiautomatic random walker segmentation (30) was applied to a downsampled version of the PDPN-positive (D2-40) channel. Segmentation of blood vessels was performed by computing vesselness features on multiple Gaussian scales similar to the method proposed by Sato et al. (31), followed by a manual thresholding step to obtain a binary image. Connected component analysis (41) was applied to both segmentations in order to identify and remove artifacts in the form of small voxel components in both foreground (spurious objects) and background (cavities). Skeletonization computed the medial axis within each vessel, applying the voxel-thinning method proposed by Chen et al. (32). We modified the algorithm in order to reduce the number of spurious branches when iterating on vessels reduced to thin sheets of voxels. Thus we account for anisotropic resolution and nonuniform vessel radius. Topology of the resulting vessel network was extracted by identification of junctions and skeleton voxels that belonged to vessel segments based on a simplified version of the definitions of Klette (33). This allows us to identify the connectivity of a voxel solely by observing its $3 \times 3 \times 3$ neighborhood and thus enables computation of the topology of the complete vessel network in a single sweep over the binary volume. Special voxel configurations that necessitate more complicated connectivity computation according to Klette are already ruled out in the postprocessing step of the segmentation. Segments at the sample boundary were marked and excluded from the subsequent analysis of parameters such as segment length. Based on the binary image obtained by segmentation in conjunction with the extracted skeleton and the topology of the vessel network characteristic features were calculated. Topological features included the connectivity of junctions, while morphological features of the vessel segments included average radius, roundness (ratio between the surface voxels with the largest and smallest distance to the medial axis in the cross section), and straightness (shortest distance between two branching points divided by the segment length).

Lymphoscintigraphy. For visualization of the whole limb lymph drainage and lymph nodes as well as assessment of lymph transport, a radioactive tracer, Technetium-99m, was injected into the web spaces between toes and fingers. Imaging was performed by γ camera, and tracer uptake into the inguinal and axillary lymph nodes was quantified 2 hours after injection to determine lymph transport.

Statistics. Per-node and per-edge properties of each vessel graph are visualized using box-and-whisker plots, with the line depicting the median. The lowest and highest data are those within 1.5 times the interquartile range of the lower and upper quartile. Outliers are displayed individually as small circles. Mann-Whitney *U* test with Bonferroni correction (for multiple comparisons) was used to compare data among groups. $P < 0.05$ was considered statistical significant. All statistical analysis was performed using SigmaPlot 11.0.

Study approval. The subject in this study was recruited through the St. George's Hospital genetic and lymphovascular clinic in the United Kingdom. Ethical approval for this study was obtained from the South West London Research Ethics Committee, London, United Kingdom (REC ref: 05/Q0803/257). Written

informed consent was obtained for the study as well as for photographs of the patient appearing in the manuscript. Ethical approval for the control skin biopsies was obtained from the ethics committee of the medical faculty of the University of Münster (ref: 2008-319-f-S). After informed consent was obtained, material not required for diagnostic purposes obtained through surgical interventions, independent from this study, served as healthy control tissue. All control biopsies were from calf skin.

Author contributions

FK and RH conceived the project, designed experiments, analyzed and interpreted data, and wrote the manuscript; DD and AS designed data analysis software, analyzed and interpreted data, and contributed to the manuscript; CD performed and analyzed experiments and contributed to the manuscript; SMA and MS contributed to the manuscript; and SB, KG, KH, PO, DV, TG, SM, XJ, and PSM provided reagents and analyzed and contributed to the manuscript.

Acknowledgments

We extend our thanks to the patient. We thank Peter Baluk and Steve P. Watson for critically reviewing and discussing the manuscript. We thank Tobias Brix for support with the volume visualization framework Voreen. This work was supported in part by grants from the DFG (SFB 656 to FK, RH, XJ, MS, AS, and KH), funding from the Cells-in-Motion Cluster of Excellence EXC 1003 (to FK, MS, XJ, and KH), and a travel grant from the Lymphatic Education and Research Network to RH.

Address correspondence to: Friedemann Kiefer, Max Planck Institute for Molecular Biomedicine, Röntgenstraße 20, D-48149 Münster, Germany. Phone: 43.251.70365.230; Email: fkiefer@gwdg.de.

1. Schulte-Merker S, Sabine A, Petrova TV. Lymphatic vascular morphogenesis in development, physiology, and disease. *J Cell Biol*. 2011;193(4):607–618.
2. Mortimer PS, Rockson SG. New developments in clinical aspects of lymphatic disease. *J Clin Invest*. 2014;124(3):915–921.
3. Alitalo K. The lymphatic vasculature in disease. *Nat Med*. 2011;17(11):1371–1380.
4. Aspelund A, Robciuc MR, Karaman S, Makinen T, Alitalo K. Lymphatic system in cardiovascular medicine. *Circ Res*. 2016;118(3):515–530.
5. Kutkut I, Meens MJ, McKee TA, Bochaton-Piallat ML, Kwak BR. Lymphatic vessels: an emerging actor in atherosclerotic plaque development. *Eur J Clin Invest*. 2015;45(1):100–108.
6. Girard JP, Moussion C, Förster R. HEVs, lymphatics and homeostatic immune cell trafficking in lymph nodes. *Nat Rev Immunol*. 2012;12(11):762–773.
7. Rockson SG, Rivera KK. Estimating the population burden of lymphedema. *Ann N Y Acad Sci*. 2008;1131:147–154.
8. Moffatt CJ, et al. Lymphoedema: an underestimated health problem. *QJM*. 2003;96(10):731–738.
9. Moffatt CJ, Keeley V, Franks PJ, Rich A, Pinnington LL. Chronic oedema: a prevalent health care problem for UK health services [published online ahead of print December 4, 2016]. *Int Wound J*. https://doi.org/10.1111/iwj.12694.
10. Greene AK, Grant FD, Slavin SA. Lower-extremity lymphedema and elevated body-mass index. *N Engl J Med*. 2012;366(22):2136–2137.
11. Newman B, et al. Possible genetic predisposition to lymphedema after breast cancer. *Lymphat Res Biol*. 2012;10(1):2–13.
12. Modi S, Stanton AW, Mortimer PS, Levick JR. Clinical assessment of human lymph flow using removal rate constants of interstitial macromolecules: a critical review of lymphoscintigraphy. *Lymphat Res Biol*. 2007;5(3):183–202.
13. Unno N, et al. A novel method of measuring human lymphatic pumping using indocyanine green fluorescence lymphography. *J Vasc Surg*. 2010;52(4):946–952.
14. Tashiro K, Yamashita S, Saito T, Iida T, Koshima I. Proximal and distal patterns: Different spreading patterns of indocyanine green lymphography in secondary lower extremity lymphedema. *J Plast Reconstr Aesthet Surg*. 2016;69(3):368–375.
15. O'Donnell TF, Rasmussen JC, Sevick-Muraca EM. New diagnostic modalities in the evaluation of lymphedema. *J Vasc Surg Venous Lymphat Disord*. 2017;5(2):261–273.
16. Chong C, et al. In vivo visualization and quantification of collecting lymphatic vessel contractility using near-infrared imaging. *Sci Rep*. 2016;6:22930.
17. Mertz J. Optical sectioning microscopy with planar or structured illumination. *Nat Methods*. 2011;8(10):811–819.
18. Keller PJ, Dodt HU. Light sheet microscopy of living or cleared specimens. *Curr Opin Neurobiol*. 2012;22(1):138–143.
19. Laviña B, Gaengel K. New imaging methods and tools to study vascular biology. *Curr Opin Hematol*. 2015;22(3):258–266.
20. Pollmann C, Hägerling R, Kiefer F. Visualization of lymphatic vessel development, growth, and function. *Adv Anat Embryol Cell Biol*. 2014;214:167–186.
21. de Medeiros G, Balázs B, Hufnagel L. Light-sheet imaging of mammalian development. *Semin Cell Dev Biol*. 2016;55:148–155.
22. Feuchtinger A, Walch A, Dobosz M. Deep tissue imaging: a review from a preclinical cancer research perspective. *Histochem Cell Biol*. 2016;146(6):781–806.
23. Kreuter A, et al. A human papillomavirus-associated disease with disseminated warts, depressed cell-mediated immunity, primary lymphedema, and anogenital dysplasia: WILD syndrome. *Arch Dermatol*. 2008;144(3):366–372.
24. Meyer-Spradow J, Ropinski T, Mensmann J, Hinrichs K. Voreen: a rapid-prototyping environment for ray-casting-based volume

visualizations. *IEEE Comput Graph Appl*. 2009;29(6):6–13.
25. Brix T, Praßni J-S, Hinrichs KH. Visualization of large volumetric multi-channel microscopy data streams on standard PCs. Cornell University Library. https://arxiv.org/abs/1407.2074. Accessed July 25, 2017.
26. Wegmann F, Ebnet K, Du Pasquier L, Vestweber D, Butz S. Endothelial adhesion molecule ESAM binds directly to the multi-domain adaptor MAGI-1 and recruits it to cell contacts. *Exp Cell Res*. 2004;300(1):121–133.
27. Schacht V, et al. T1alpha/podoplanin deficiency disrupts normal lymphatic vasculature formation and causes lymphedema. *EMBO J*. 2003;22(14):3546–3556.
28. Wigle JT, Oliver G. Prox1 function is required for the development of the murine lymphatic system. *Cell*. 1999;98(6):769–778.
29. Prevo R, Banerji S, Ferguson DJ, Clasper S, Jackson DG. Mouse LYVE-1 is an endocytic receptor for hyaluronan in lymphatic endothelium. *J Biol Chem*. 2001;276(22):19420–19430.
30. Prassni JS, Ropinski T, Hinrichs K. Uncertainty-aware guided volume segmentation. *IEEE Trans Vis Comput Graph*. 2010;16(6):1358–1365.
31. Sato Y, et al. Three-dimensional multi-scale line filter for segmentation and visualization of curvilinear structures in medical images. *Med Image Anal*. 1998;2(2):143–168.
32. Chen Y, Drechsler K, Zhao W, Laura CO. A thinning-based liver vessel skeletonization method. *2011 International Conference on Internet Computing and Information Services*. 2011:152–155.
33. Klette G. Branch voxels and junctions in 3D skeletons. *Lect Notes Comput Sc*. 2006;4040:34–44.
34. Renier N, Wu Z, Simon DJ, Yang J, Ariel P, Tessier-Lavigne M. iDISCO: a simple, rapid method to immunolabel large tissue samples for volume imaging. *Cell*. 2014;159(4):896–910.
35. Hama H, et al. ScaleS: an optical clearing palette for biological imaging. *Nat Neurosci*. 2015;18(10):1518–1529.
36. Susaki EA, Ueda HR. Whole-body and whole-organ clearing and imaging techniques with single-cell resolution: toward organism-level systems biology in mammals. *Cell Chem Biol*. 2016;23(1):137–157.
37. Schmid B, et al. High-speed panoramic light-sheet microscopy reveals global endodermal cell dynamics. *Nat Commun*. 2013;4:2207.
38. Connell FC, et al. The classification and diagnostic algorithm for primary lymphatic dysplasia: an update from 2010 to include molecular findings. *Clin Genet*. 2013;84(4):303–314.
39. Hägerling R, et al. A novel multistep mechanism for initial lymphangiogenesis in mouse embryos based on ultramicroscopy. *EMBO J*. 2013;32(5):629–644.
40. Orlich M, Kiefer F. A qualitative comparison of ten tissue clearing techniques [published online ahead of May 12, 2017]. *Histol Histopathol*. https:doi.org/10.14670/HH-11-903.
41. Isenburg M, Shewchuk J. Streaming connected component computation for trillion voxel images. Workshop on Massive Data Algorithmics. June 11, 2009.